ADVANCED THEORY AND SIMULATIONS
www.advtheorysimul.com

Conductive Tracks in Carbon Implanted Titania Nanotubes: Atomic-Scale Insights from Experimentally Based Ab Initio Molecular Dynamics Modeling

Alexander Holm, Astrid Kupferer, Stephan Mändl, Andriy Lotnyk, and Stefan G. Mayr**

Ion implantation of titania nanotubes is a highly versatile approach for tailoring structural and electrical properties. While recently self-organized nanoscale compositional patterning has been reported, the atomistic foundations and impact on electronic structure are not established at this point. To study these aspects, ab initio molecular dynamic simulations based on atomic compositions in C implanted titania nanotubes according to elastic recoil detection analysis are employed. Consistent with experimental data, carbon accumulates in chainlike precipitates, which are favorable for enhancing conductivity, as revealed by density-functional theory electronic ground states calculations are demonstrated.

1. Introduction

TiO_2 nanotube arrays constitute a multifunctional materials system that has attracted significant interest in a broad range of applications during the past decade, ranging from solar cells and photocatalysts to sensors, implants and tissue cultivation platforms.[1–7] This versatility across different scientific disciplines can be traced back to highly tunable structural and electronic properties that affect physics, chemistry as well as biomedical features of TiO_2 nanotubes. While key structure–property relationships have been unveiled, recipes for tailored nanotube synthesis have been proposed which include anodization[8] as well as post-anodization modification.[9–12] Among those, ion implantation is showing promise as a tool for precisely tailoring structural and electronic properties.[13–16] This also includes nanoscale chainlike compositional patterning, which arises upon carbon ion implantation and will be in the center of focus of the present manuscript.

Within the framework of driven alloys, we previously derived a continuum model based on the Cahn and Hillard approach[17] complemented with a linear stability analysis[18,19] to describe the dynamical pattern formation (cf. **Figure 1**) observed in C implanted titania nanotubes.[20] The atomic species detected in the nanotube arrays by scanning transmission electron microscopy (STEM) are Ti, C, O, and F.[20] Additionally, the present study takes hardly localizable H into account which is abundant in the samples. Owing to similar atomic sizes among C, O, and F and their amorphous arrangements combined with sample thicknesses beyond few atomic layers, deriving short-range orders suitable for electronic structure calculations from measurements is currently not accessible. Understanding the atomic structure at short-range, however, is necessary for predicting the electronic structure in the C implanted titania nanotubes.

Consequently, in the present study we unveil the atomic scale kinetics of the previously described dynamical pattern formation using ab initio molecular dynamics (AIMD) based on irradiation-enhanced diffusion and elastic recoil detection analysis (ERDA). We chose the AIMD approach because it allows for predicting trajectories of systems which comprise up to a few hundred atoms over short time scales while providing accurate atomic interactions. In the early stages, the approach has proven in the simulation of liquids and quenches using Si and SiO_2,[21–23] comparable to kinetics in irradiation-induced thermal spikes.[24] In the present study, the simulations were performed with an AIMD setup implemented in the CP2K code suite,[25] which has been used for different recent studies on TiO_2 as well.[26–28]

The starting point in this work is the creation of an amorphous simulation cell which respects the stoichiometry obtained from ERDA on implanted titania nanotube arrays. From this point on, trajectories of the system are calculated which represent a high diffusivity; an aspect which is important for time propagation of the presently studied system. It is established that ion implantation induces materials transport, that is radiation enhanced diffusion[20,24] mediated by i) thermally activated and ii) ballistic mechanisms. While (i) and (ii) act on different length scales,

A. Holm, A. Kupferer, S. Mändl, A. Lotnyk, S. G. Mayr
Leibniz Institute of Surface Engineering (IOM)
Permoserstr.15, Leipzig 04318, Germany
E-mail: alexander.holm@iom-leipzig.de; stefan.mayr@iom-leipzig.de
A. Holm, A. Kupferer, S. G. Mayr
Division of Surface Physics
Faculty of Physics and Earth Sciences
University of Leipzig
Linnestr. 5, Leipzig 04103, Germany

The ORCID identification number(s) for the author(s) of this article can be found under https://doi.org/10.1002/adts.202200063

DOI: 10.1002/adts.202200063

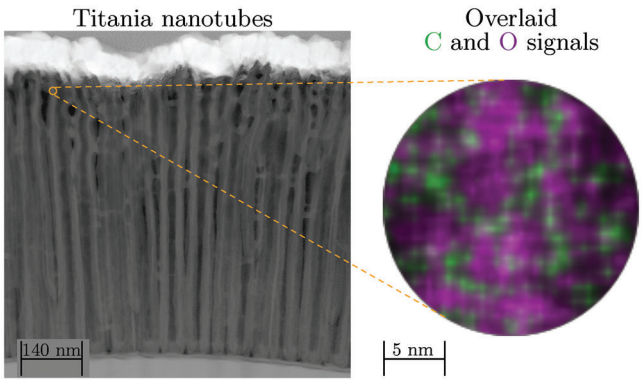

Figure 1. High-angle annular dark-field (HAADF) and scanning transmission electron microscopy(STEM) images, resolved for C and O, of C implanted titania nanotubes. The chemical mapping is achieved with energy-dispersive X-ray spectroscopy (EDX). As can be deduced from comparing the C and O STEM data, a pattern formation driven by ion implantation takes place. This effect was also observed within a coarse-grained continuum picture.[20]

their prevalence can be linked to thermal-spike-like regions and recoils within collision cascades, respectively. In view of these distinct mechanisms, selected structures along the trajectories are quenched and subsequently structurally relaxed to study electronic ground state properties based on density functional theory (DFT) and eventually discuss conductivity.

We will show that carbon arranges in nanoscale chainlike precipitates that establish conductive tracks for enhancing electrical conductivity. This extends our understanding of implantation-induced phase tuning in titania nanotubes to an atomistic picture.

2. Results and Discussion

2.1. Simulation Cell Based on Elastic Recoil Detection Analysis

ERDA was performed over the entire height of the implanted nanotubes (≈570 nm). Except for inhomogeneities near surface and substrate, the atomic composition is relatively homogeneous in the region where most of the energy dissipates during implantation (cf. Supporting Information). Therefore, the average atomic composition is used as a basis to study overall trends. The average stoichiometry revealed by ERDA is 33.8% Ti, 1.9% F, 54.1% O, 7.1% C, and 3.1% H. This stoichiometry was implemented in the amorphous simulation cell by replacing Ti and O sites with corresponding defect atoms in such a way that these defects were distributed as homogeneously as possible and the average distance between the nearest defect sites was maximized. Based on this scheme, we tried to exclude initially unknown effects of particular defect accumulations and resulting short-range orders. Additionally, the overall charge of the simulation is balanced according to the formal oxidation states of the employed elements (Ti +4, F −1, O −2, C −4, H +1), which translates to a representative $Ti_{72}F_4O_{116}C_{15}H_8$ configuration, comprising 215 atoms in total. The resulting initial distribution of H, C, and F without the surrounding Ti and O atoms is schematically shown in **Figure 2**a).

2.2. AIMD Trajectory and Evolution of the Short-Range Order

Generally, the process of ion implantation alters the target materials in different ways and across different scales, one aspect being the diffusivity enhanced by the radiation (see for example refs. [30–32] and references therein). Furthermore, diffusion in irradiated systems needs to be understood in terms of two distinct mechanisms and their interplay. Short-range random walk type diffusion above the critical temperature of the mode coupling theory[33] ($T_C \approx 1492$ K for TiO_2[24]) in thermal spikes and long-range ballistic diffusion due to collisions involving high kinetic energies.[34] Both these mechanisms contribute to viscous flow in the irradiated glassy system, as shown previously.[15,16,20] Especially at lower temperatures, viscous flow prevails as a manifestation of shear instabilities due to irradiation-induced point defects, namely, shear transformation zones.[35,36] These effects of flow and enhanced diffusivity on the atomic level are imposed on the AIMD trajectories by increasing the canonical ensemble temperature to 3000 K. This regime is chosen, as it compares well with those temperatures obtained by previous studies on irradiation-induced thermal spikes in amorphous TiO_2 on short time scales.[24]

In the course of the simulations, an unambiguous trend can be identified which predicts preferred short-range orders of neighboring C atoms. This tendency culminates in the formation of chainlike C precipitates. This catenation is typical for C and as well consistent with recently reported results based on STEM measurements,[20] where accumulation of C in domains is observed, assuming interconnection of these domains via network-like structures. However, a detailed domain shape resolved on the atomic level is experimentally hardly accessible. The C chain formation process was also confirmed for smaller amorphous systems accommodating 98 atoms, which is shown in the Supporting Information.

The highly mobile H atoms in the simulation cell are observed in different intermediate metastable states, such as H_2, OH, and CH groups. After quenching, the H atoms reside predominantly bonded to C or O. The F atoms, on the other hand, remain bound to Ti throughout the simulations. Overall, the amorphous structure of the simulation cell persists, as can be seen from the radial distribution functions and Voronoi-derived neighborhood coordinations presented in the Supporting Information. Particularly, the Ti neighborhood coordinations reveal a relevant percentage of fourfold (20 %) and fivefold (37.5 %) coordinated Ti, compared to sixfold (37.5 %) coordinated Ti occurring in crystalline TiO_2 phases. The observed sixfold coordinated Ti resembles unconnected distorted octahedral structures with neighboring atoms. The Ti−O bond lengths spread within a range of ±0.2Å around those observed in crystalline phases, which is an additional manifestation of the amorphous character.[26]

For further discussions on distinctive emerging configurations, especially for subsequent DFT ground state calculations, two exemplary cases along the trajectory of the canonical ensemble at elevated temperature are chosen to be quenched. The decision about the two to-be-quenched cases was made in light of the two competing diffusion mechanisms: thermal activation and repeated quenches may drive the system toward thermodynamically more equilibrated ordered states, whereas ballistic contributions impose randomization by continuously disrupting

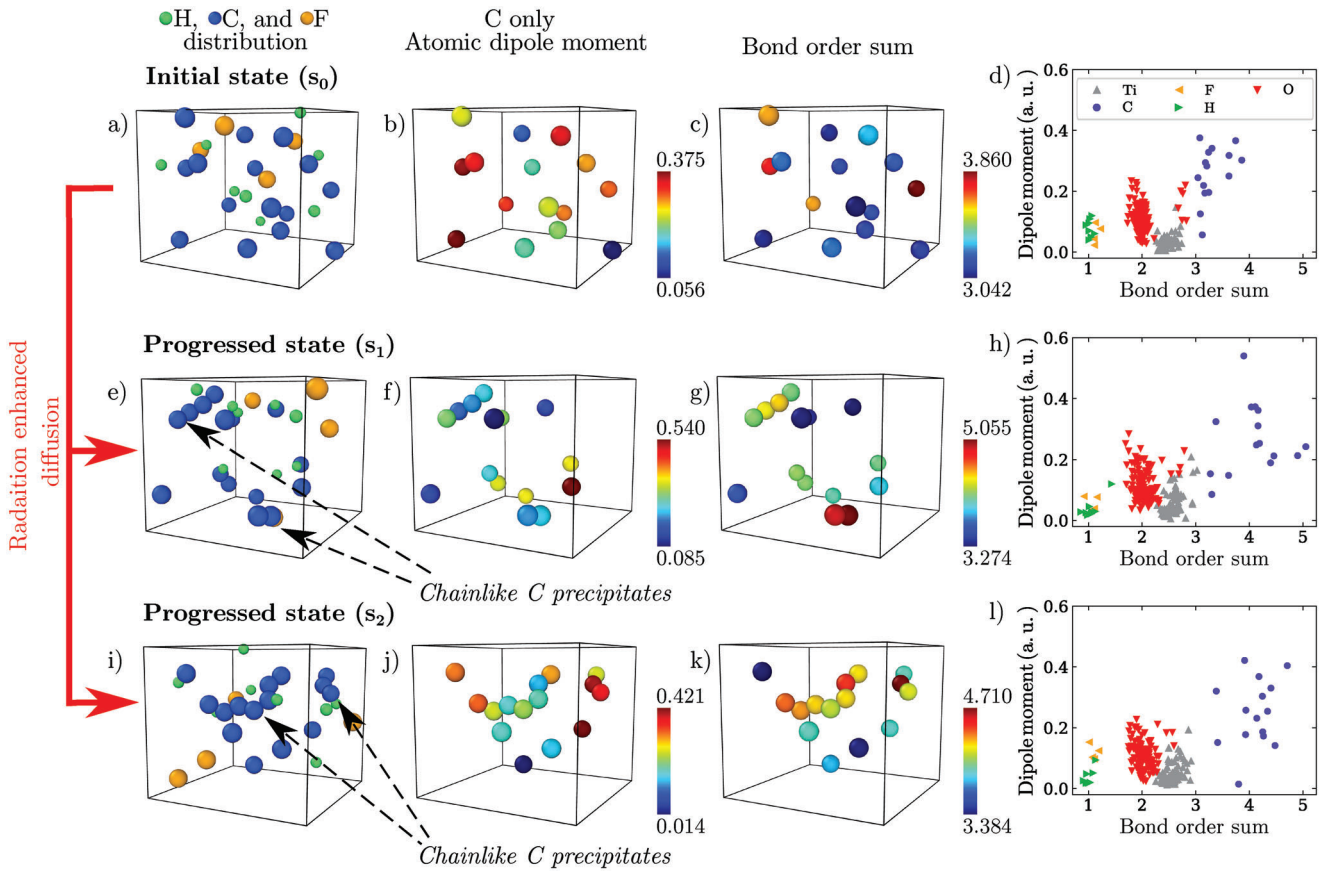

Figure 2. a) Molecular dynamics snapshot[29] of the simulation cell at the initial state s_0, sowing the H, C, and F defects only, which are embedded in the hidden amorphous TiO_2 matrix, b) dipole moments on the C atoms, c) bond order sums of the C atoms, and d) scatter plot to show the connection between atomic dipole moment and bond order sum. Below, snapshots and plots of the same properties for (e–h) progressed state s_1 with smaller unconnected C precipitates and (i–l) progressed state s_2 accommodating an extended chainlike C precipitates of seven atoms.

emerged orders. In this sense, the first case resembles a configuration along the trajectory obtained after ≈2 ps which accommodates smaller C precipitates: a chain of four atoms and two pairs of connected C atoms (shown in Figure 2e, further on referred to as s_1). Compared to this, the second case resembles a configuration obtained after ≈5 ps which accommodates a more extended C chain of seven atoms (shown in Figure 2i and further on referred to as s_2). The parameters for the exponential quench temperature curve were fitted directly to the cooling rate observed in thermal spikes in amorphous TiO_2.[24]

2.3. Enthalpy and Dipole Moments

A first measure to discuss the observed structures are the calculated ground state energies. The simulation cells of all three considered cases, comprising the initial state (denoted by s_0) and both the propagated states with varying C chain lengths, were geometrically optimized. Without stresses and therefore mechanical contributions, the enthalpy difference with respect to the initial state $s_0 \rightarrow s_{1/2}$ becomes equivalent to the internal energy difference

$$\Delta H(s_0 \rightarrow s_{1/2}) = \Delta U(s_0 \rightarrow s_{1/2}) = U(s_{1/2}) - U(s_0) \quad (1)$$

with $U(s_a)$ referring to the calculated ground state energies.

Both employed DFT approaches confirm that the states which accommodate the chainlike C structures are energetically more favorable. The PW-SP+U (cf. Experimental Section) approach predicts −112 meV atom^{-1} for the progressed state with smaller precipitates (cf. Figure 2e) and −160 meV atom^{-1} for the state with the larger C chain (cf. Figure 2i), whereas the GPW (cf. Experimental Section) approach predicts −68 meV atom^{-1} for the first and −110 meV atom^{-1} for the latter case. Discrepancies result from differences in the electronic ground states, as pointed out in Section 4.

These lower ground state energies can be considered as one aspect for the formation of the C precipitates. Driven by diffusion, the simulation cell is allowed to explore the configuration space and maintain structures which are energetically favorable. A different mechanism for the formation of C precipitates to be discussed is van der Waals interactions between atomic dipoles. For evaluating these dispersion effects,[37] DFT ground states were calculated both with this option enabled and disabled. The contribution of dispersion correction to the averaged total energy per atom is ≈−140 meV atom^{-1} (PW−SP+U) to −165 meV atom^{-1} (GPW) (varying due to differently approximated electronic ground states, discussed in Section 4). Estimates of the occurring atomic dipole moments are derived

from the DFT ground state densities with the CHARGEMOL[38] post processor, shown in Figure 2. The atomic dipole character varies strongly between different C atoms. This is not only caused by different atomic environments, but coordination of the surrounding atoms as well. For example, in Figure 2b, the C atoms with the highest and lowest dipole moment both have three Ti neighbors. The exact distribution and the development of atomic dipoles in the amorphous system is, therefore, hardly predictable. However, one observes that: i) C bonding to a single O; ii) C bonding to C without surrounding oxygen; and iii) C at the tail ends of chainlike precipitates are structures that promote higher C atomic dipole moments. Remarkably, the C precipitates are predominantly surrounded by Ti (except for the tail ends), which compares well to experimentally observed compositional patterning as an expression of segregation between C and O subsystems.[20]

The presence of C precipitates in irradiated titania nanotubes has been detected in other experiments as well. X-ray photoelectron spectroscopy (XPS) reveals a significant proportion sp^3 C–C bonds (shown in the Supporting Information). An implantation-caused increase in the number of C precipitates can be deduced from Raman spectroscopy as well.[16] As discussed in this study, a shift of the G peak indicates a transition from nanocrystalline graphite (presumably residues of the organic electrolyte of the production process) to graphite.

In the simulations, we observe that the average bond order sum of C increases with increasing size of the chainlike C precipitates (cf. Supporting Information). This correlates with increased bond orders among the clustering C atoms. In these configurations, the bond orders for C distribute among fractional bonds to surrounding Ti (≈ 0.5) atoms and adjacent C atoms (≈ 1.5). Therefore, surrounding Ti seemingly interferes with the C bond order. It might be subject to further studies to clarify whether it drives the enclosing C atoms in the precipitates toward double bonds, prevents them from forming or stabilizes the fractional bond order.

Based on these results one can conclude the simplified mechanism that C atoms attract each other via i) atomic dipole interactions and ii) a drive toward energetically more favorable C bonds and higher C bond order sums.

2.4. Electronic Structure and Electronic Conductivity

For a more in depth electronic structure discussion of the quenched and geometrically optimized configurations, the corresponding projected densities of states (PDOS) are calculated. **Figure 3** shows the PDOS resolved for the atomic species obtained from a) PW-SP+U and b) GPW calculations (PDOS, resolved for the atomic orbitals, are presented in the Supporting Information).

Comparing the electronic structures obtained from both DFT approaches, one observes multiple electronic states embedded in the energy region associated with the band gap in pristine amorphous TiO_2.[39,40] Due to strong modifications of the electronic structure by the employed defects, the concepts of conduction band, valence band, and band gap, might not necessarily transfer to the present system. However, the terms are subsequently

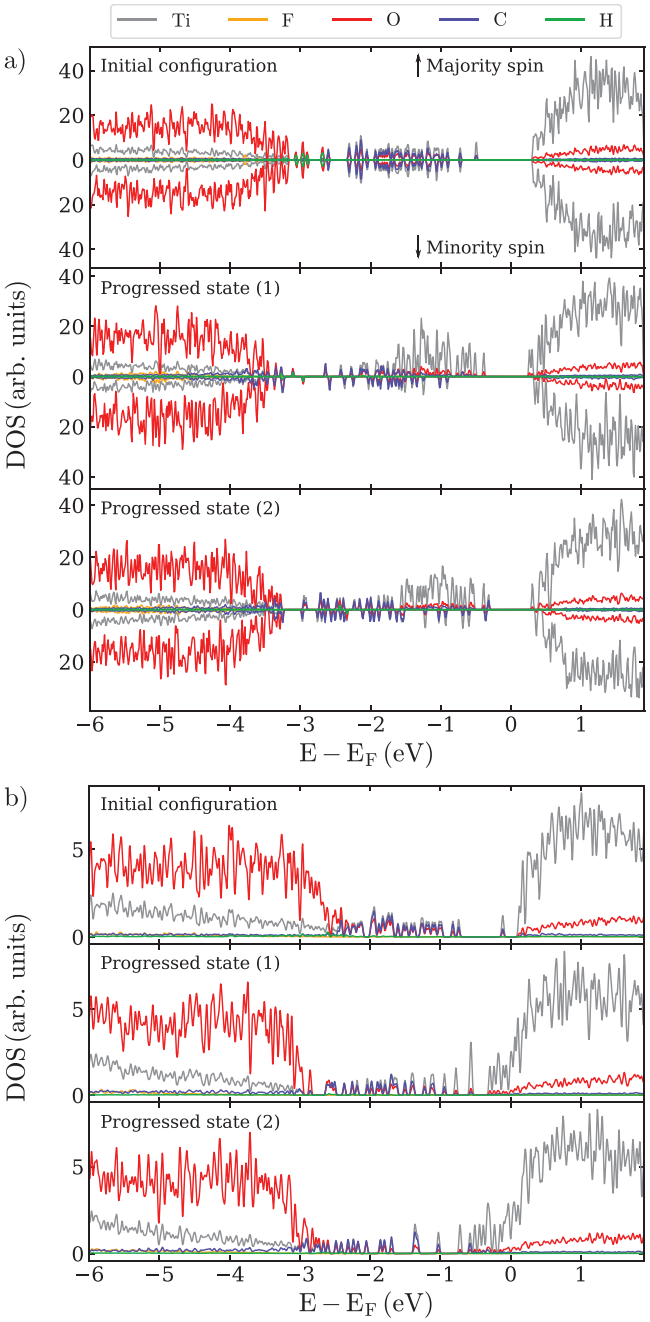

Figure 3. Projected densities of states of the initial configuration and both progressed states, described in Section 2.2, after quenching and geometry optimization. a) The results of the spin polarized PW-SP+U calculations and b) those of the GPW calculations.

adopted to compare differences between the presently studied systems to pure amorphous TiO_2.

Both, PW-SP+U and GPW, show the accumulation of energetically adjacent C states, which correlates with the chain length. With increasing amount of C in precipitates, these C states shift toward the valence band edge, namely lower energies. Also observed are Ti states inside the former band gap, which show magnetic polarization (in the case of PW-SP+U). The Ti

atoms connected to these states reveal ≈ 18 % smaller partial charges, which is a fingerprint of Ti^{3+} states.[41] PW-SP+U predicts these Ti states in the energy range close to C intra band gap states, whereas the Ti^{3+} states predicted by GPW are smeared out around the Fermi energy close to the conduction band edge.

This observation already accounts for the main difference between the PDOS calculated with the different DFT approximations: the energies of the defect states relative to the band edges (cf. Section 4). In contrast to the smeared density of states around the conduction band edge, enclosing the Fermi energy (predicted by GPW), there remains a small gap between the highest occupied defect states and the conduction band edge around the Fermi energy in the PW-SP+U density of states of ≈0.56 eV. Nonetheless, both DFT approaches predict the same overall trends as pointed out above and the energy range of the deep C defects and Ti^{3+} states compare to previous calculations by Di Valentin et al.[41–43] or Pham and Wang[44] on the influence of point defects in crystalline and amorphous TiO_2 systems, respectively.

The resulting PDOS of the implanted titania nanotubes lead to conclusions about the conductivity. First, at 0 K the energy difference between the highest occupied state and the lowest unoccupied state is significantly smaller compared to pure amorphous TiO_2 (PW-SP+U) or there is no gap at all, since the Fermi energy is inside the Ti 3d band (GPW). The number of thermally excited electrons increases approximately exponentially with decreasing energy gap at constant temperature.[45] This leads to a significantly larger number of electrons in the Ti 3d states and, consequently, unoccupied defect states inside the band gap, compared to pure amorphous TiO_2. This availability of unoccupied states enables, second, variable range hopping[46] as a fundamental mechanism for charge transport. The charge transfer rate increases with smaller separation between two sites, which includes spatial distance and energy differences.[47] Both these criteria are matched for the presently observed C chains: electronic states with small energy differences (in the range of 60 meV) connected via adjacent atomic sites.

Preliminary experimental results imply that resistivity in titania nanotubes decreases about 3 orders of magnitude due to ion implantation at similar energies and fluences used in this study.[20] A full account on these experiments will be published in the future.[48]

Pristine (i.e., unimplanted) amorphous samples can be described based on the chemical reactions underlying the electrochemical anodization process to produce titania nanotube arrays.[8,49–51] However, solely from concentration profiles, without information about involved atomic transport mechanisms, spatially resolved short-range orders required for electronic structure calculations cannot be directly derived from the results.

3. Conclusion

Overall, we complement our previously derived coarse-grained continuum picture[20] with in-depth atomistic simulations on C precipitation in amorphous titania nanotubes. This substantiates that ion implantation achieves nanoscale phase tuning in these amorphous systems. Crucial for this is controlling the depth profile of dissipated energy (either kinetic and/or stored in structural defects) by an interplay of ion energy, species, and fluence.[16]

With a combined experimental and theoretical approach, we improve the explanations of two effects observed in C implanted titania nanotubes: i) formation of C patterns; and ii) enhanced conductivity. Based on ERDA, which serve as starting point for atomistic simulations, comprehensive information about atomic compositions in these titania nanotobe systems is gained.

Trajectories at elevated temperature are calculated to capture the effects of irradiation-enhanced diffusion, along which the tendency of C atoms to form precipitates is observed. For this formation process, a mechanism of dipole interactions and drive toward energetically favorable C double bonds is presented and discussed. Eventually, in the progressed, quenched, and structurally relaxed simulation cells, electronic structures are identified that explain enhanced conductivity based on the variable range hopping charge transport model.

4. Experimental Section

The production of titania nanotubes and implantation has already been presented in different experimental sections,[16,20] and can additionally be found in the Supporting Information. In brief, the titania nanotubes of ≈ 1 μm height on a 0.1 mm thick Ti foil, were produced by electrochemical anodization. They were twice implanted with ^{12}C: first at 60 keV, followed by 150 keV each for a fluence of 1×10^{16} cm^{-2}. This procedure was chosen to achieve a more homogeneous implantation profile, evaluated with ERDA. The details about this measurement technique can be found in the Supporting Information as well.

The simulation cells carrying the amorphous TiO_2 structure as starting point for this study originate from classical molecular dynamics (MD) performed with LAMMPS.[52] Those employ a melt-quench protocol similar to that described in ref. [24] with a quench rate of 100 K ps^{-1}. For the MD simulations, the atomic interactions were modeled with the Matsui–Akaogi parametrization of the combined Coulomb and Buckingham potential model.[53]

The AIMD trajectories were obtained by propagating the prepared simulation cells along the Born–Oppenheimer potential energy surface, according to the implementation in the CP2K code suite.[25] The time step throughout the simulations was 0.5 fs, adopting to elevated temperatures and the light mass of hydrogen. The canonical ensemble was realized with a Nose–Hoover thermostat,[54–56] with a chain length of three and a time coupling constant equivalent to 1000 fs. During the quenches, a Langevin thermostat[57] with a gamma parameter of 0.01 fs^{-1} was employed to shape the decaying temperature curve, provided by the temperature annealing function. After every MD step, the forces were derived from the electronic ground state of the corresponding new configuration.

The DFT groundstates were calculated based on the combined Gaussian and plane wave (GPW) basis sets approach, implemented in quickstep[58] of the CP2K suite. For this approach, the present study employed double-zeta valence, molecular optimized, short-range, Goedecker–Teter–Hutter (GTH) basis sets and GTH pseudopotentials, optimized for Perdew–Becke–Ernzerhof (PBE) functionals.[59–63] Both plane wave and Gaussian reference grid cut-offs of 5442.27 and 680.28 eV, respectively, showed sufficiently accurate convergence of ≈2.64×10^{-4} eV $atom^{-1}$ with respect to total energy. The energy convergence tolerances were the default of 1.36×10^{-4} eV during AIMD runs and 1.36×10^{-7} eV for the subsequently performed density of states groundstate calculations.

Complementary to the DFT approach used for the AIMD simulations, an additional approach was employed to capture the effect of spin polarization and Hubbard correction. The fully spin polarized calculations were performed with the plane approach (subsequently referred to as PW-SP+U), implemented in pwscf[64] of the QuantumESPRESSO suite. The simulations employed projector augmented wave (PAW) pseudopotentials,[65] with wave function cut-off energies of 1088.45 and 7483.13 eV for the density, respectively. A correction of the self-interaction

error for the Ti–O subsystem was approximated by applying the DFT+U scheme.[66] Previous studies demonstrated that a DFT+U correction applied to the Ti 3d orbitals only was not leading to the reasonable results.[67,68] Therefore, a Hubbard U value of 5 eV was incorporated to the O 2p and 3.3 eV to the Ti 3d orbitals, referencing a study[69] on intrinsic defects in crystalline TiO_2 based on a computational framework close to the presently employed setup in pwscf. A comprehensive evaluation of the remaining correction terms corresponding to the H, C, and F species in the amorphous arrangements leads beyond the scope of this work. The energy convergence tolerance for the PW-SP+U calculations was 1.36×10^{-7} eV.

Given the different underlying approximations presented, it was expectable that both approaches generate slightly different electronic ground states due to: i) the effect of spin-polarization on the PW-SP+U exchange-correlation (EX) functional; ii) the Hubbard correction in PW-SP+U; iii) the different representations of wave functions (plane waves[64] versus combined Gaussian and plane waves[25]); and iv) the different types and default optimizations of the pseudopotentials (PAW vs GTH and Gaussian basis sets for valence electrons). As shown in Section 2.3, this consequently effects ground state energies resulting from both approaches, which differ in the range of a few tens of meV.

Both the employed DFT approaches use: i) **k**-point sampling in reciprocal space at the Γ-point only, due to the large expansion of the simulation cell and sufficiently accurate energies compared to a finer decompositions of the reciprocal space; ii) generalized-gradient approximation EX functionals of PBE type;[70] iii) van der Waals correction schemes, which were implemented according to Grimme et al.;[37,71] and iv) the Broyden–Fletcher–Goldfarb-Shanno[72–75] algorithm for geometry optimization toward the ground states. During geometry optimization, the atoms in the respective simulation cells were allowed to adept without constraints to minimize interatomic forces. The volumes of the amorphous simulation cells were optimized to adept to vanishing external pressure while maintaining angles between the cell vectors. The maximum average force per atom after the PW-SP+U structure optimizations was 3.6×10^{-4} and 6.2×10^{-4} eV Å^{-1} after the optimizations with GPW, respectively.

From the electronic ground state densities, dipole moments and bond orders in the relaxed simulation cells were derived with CHARGEMOL.[38,76,77]

Supporting Information

Supporting Information is available from the Wiley Online Library or from the author.

Acknowledgements

The computations were performed at the Center for Information Services and High Performance Computing (ZIH) at TU Dresden. The authors acknowledge funding in parts by the European Union, ESF (European Social Fund, funding number 100316844), the German Ministry of Science and Education (BMBF), project EYECULTURE, FKZ 161A574C/031A574C, as well as the Saxon State Ministry for Science and the Arts (SMWK), grant number 100331694 (MUDIPlex). The ERDA measurements were carried out at IBC at the Helmholtz-Zentrum Dresden-Rossendorf e. V., a member of the Helmholtz Association and the authors would like to thank Dr. Frans Munnik for doing the analysis. The authors also acknowledge Dietmar Hirsch for measuring XPS.

Open access funding enabled and organized by Projekt DEAL.

Conflict of Interest

The authors declare no conflict of interest.

Data Availability Statement

The data that support the findings of this study are available from the corresponding author upon reasonable request.

Keywords

ab initio molecular dynamics, conductive carbon tracks, density functional theory, experiment and modeling, functional nanomaterials, ion implantation, titania nanotubes

Received: February 1, 2022
Revised: February 28, 2022
Published online: March 11, 2022

[1] J. M. Macak, H. Tsuchiya, L. Taveira, S. Aldabergerova, P. Schmuki, *Angew. Chem., Int. Ed.* **2005**, *44*, 7463.
[2] Y. Liu, H. Song, Z. Bei, L. Zhou, C. Zhao, B. S. Ooi, Q. Gan, *Nano Energy* **2021**, *84*, 105872.
[3] I. Paramasivam, H. Jha, N. Liu, P. Schmuki, *Small* **2012**, *8*, 3073.
[4] X. Wang, X. Chen, D. Zhang, J. Chen, P. Deng, Z. Zhong, Q. Xiang, J. Li, F. Li, Y. Liao, *ACS Sensors* **2019**, *4*, 2429.
[5] S. Wen, X. Gu, X. Ding, P. Dai, D. Zhang, L. Li, D. Liu, X. Zhao, J. Yang, *Adv. Funct. Mater.* **2021**, *32*, 2106751.
[6] J. Hou, Z. Xiao, Z. Liu, H. Zhao, Y. Zhu, L. Guo, Z. Zhang, R. O. Ritchie, Y. Wei, X. Deng, *Adv. Mater.* **2021**, *33*, 2103727.
[7] V. Dallacasagrande, M. Zink, S. Huth, A. Jakob, M. Müller, A. Reichenbach, J. A. Käs, S. G. Mayr, *Adv. Mater.* **2012**, *24*, 2399.
[8] P. Roy, S. Berger, P. Schmuki, *Angew. Chem., Int. Ed.* **2011**, *50*, 2904.
[9] S. P. Albu, A. Ghicov, S. Aldabergenova, P. Drechsel, D. LeClere, G. E. Thompson, J. M. Macak, P. Schmuki, *Adv. Mater.* **2008**, *20*, 4135.
[10] J. H. Park, S. Kim, A. J. Bard, *Nano Lett.* **2006**, *6*, 24.
[11] Y. Lu, J. Wang, Y. Chen, X. Zheng, H. Yao, S. Mathur, Z. Hong, *Adv. Funct. Mater.* **2021**, *31*, 2009605.
[12] N. Khaliq, M. A. Rasheed, M. Khan, M. Maqbool, M. Ahmad, S. Karim, A. Nisar, P. Schmuki, S. O. Cho, G. Ali, *ACS Appl. Mater. Interfaces* **2021**, *13*, 3653.
[13] A. Ghicov, J. M. Macak, H. Tsuchiya, J. Kunze, V. Häublein, L. Frey, P. Schmuki, *Nano Lett.* **2006**, *6*, 1080.
[14] X. Zhou, V. Häublein, N. Liu, N. T. Nguyen, E. M. Zolnhofer, H. Tsuchiya, M. S. Killian, K. Meyer, L. Frey, P. Schmuki, *Angew. Chem., Int. Ed.* **2016**, *55*, 3763.
[15] A. Kupferer, S. Mändl, S. G. Mayr, *Mater. Res. Lett.* **2021**, *9*, 483.
[16] A. Kupferer, M. Mensing, J. Lehnert, S. Mändl, S. G. Mayr, *Nanomaterials* **2021**, *11*, 2458.
[17] J. W. Cahn, J. E. Hilliard, *J. Chem. Phys.* **1958**, *28*, 258.
[18] P. C. Hohenberg, B. I. Halperin, *Rev. Mod. Phys.* **1977**, *49*, 435.
[19] R. A. Enrique, P. Bellon, *Phys. Rev. Lett.* **2000**, *84*, 2885.
[20] A. Kupferer, A. Holm, A. Lotnyk, S. Mändl, S. G. Mayr, *Adv. Funct. Mater.* **2021**, *31*, 2104250.
[21] J. Sarnthein, A. Pasquarello, R. Car, *Phys. Rev. B* **1995**, *52*, 12690.
[22] J. .Sarnthein, A. Pasquarello, R. Car, *Phys. Rev. Lett.* **1995**, *74*, 4682.
[23] R. Car, M. Parrinello, *Phys. Rev. Lett.* **1988**, *60*, 204.
[24] A. Holm, S. G. Mayr, *Phys. Rev. B* **2021**, *103*, 174201.
[25] T. D. Kühne, M. Iannuzzi, M. D. Ben, V. V. Rybkin, P. Seewald, F. Stein, T. Laino, R. Z. Khaliullin, O. Schütt, F. Schiffmann, D. Golze, J. Wilhelm, S. Chulkov, M. H. Bani-Hashemian, V. Weber, U. Borštnik, M. Taillefumier, A. S. Jakobovits, A. Lazzaro, H. Pabst, T. Müller, R. Schade, M. Guidon, S. Andermatt, N. Holmberg, G. K. Schenter, A. Hehn, A. Bussy, F. Belleflamme, G. Tabacchi, et al., *J. Chem. Phys.* **2020**, *152*, 194103.
[26] Z. Guo, F. Ambrosio, A. Pasquarello, *J. Mater. Chem. A* **2018**, *6*, 11804.
[27] G. Zollo, K. Hermansson, L. Agosta, *Appl. Surf. Sci.* **2021**, *550*, 149354.
[28] C. Kamal, N. Stenberg, L. E. Walle, D. Ragazzon, A. Borg, P. Uvdal, N. V. Skorodumova, M. Odelius, A. Sandell, *Phys. Rev. Lett.* **2021**, *126*, 016102.

[29] A. Stukowski, *Modell. Simul. Mater. Sci. Eng.* **2009**, *18*, 015012.
[30] R. S. Averback, T. D. D. L. Rubia, *Solid State Phys. (New York. 1955)* **1997**, *51*, 281.
[31] F. Faupel, W. Frank, M.-P. Macht, H. Mehrer, V. Naundorf, K. Rätzke, H. R. Schober, S. K. Sharma, H. Teichler, *Rev. Mod. Phys.* **2003**, *75*, 237.
[32] K. Nordlund, S. J. Zinkle, A. E. Sand, F. Granberg, R. S. Averback, R. E. Stoller, T. Suzudo, L. Malerba, F. Banhart, W. J. Weber, F. Willaime, S. L. Dudarev, D. Simeone, *J. Nucl. Mater.* **2018**, *512*, 450.
[33] W. Götze, *Complex Dynamics of Glass-Forming Liquids: A Mode-coupling Theory*, Vol. *143*, Oxford University Press, Oxford **2008**.
[34] R. A. Enrique, K. Nordlund, R. S. Averback, P. Bellon, *J. Appl. Phys.* **2003**, *93*, 2917.
[35] S. G. Mayr, Y. Ashkenazy, K. Albe, R. S. Averback, *Phys. Rev. Lett.* **2003**, *90*, 055505.
[36] S. G. Mayr, *Phys. Rev. Lett.* **2006**, *97*, 195501.
[37] S. Grimme, J. Antony, S. Ehrlich, H. Krieg, *J. Chem. Phys.* **2010**, *132*, 154104.
[38] T. A. Manz, N. G. Limas, *RSC Adv.* **2016**, *6*, 47771.
[39] S. K. Deb, *Solid State Commun.* **1972**, *11*, 713.
[40] M. Landmann, T. Köhler, S. Köppen, E. Rauls, T. Frauenheim, W. G. Schmidt, *Phys. Rev. B* **2012**, *86*, 064201.
[41] C. D. Valentin, G. Pacchioni, A. Selloni, *J. Phys. Chem. C* **2009**, *113*, 20543.
[42] C. D. Valentin, G. Pacchioni, A. Selloni, *Chem. Mater.* **2005**, *17*, 6656.
[43] C. D. Valentin, G. Pacchioni, *Catal. Today* **2013**, *206*, 12.
[44] H. H. Pham, L.-W. Wang, *Phys. Chem. Chem. Phys.* **2015**, *17*, 11908.
[45] M. Grundmann, *Physics of Semiconductors*, Vol. *11*, Springer, Berlin **2010**.
[46] N. F. Mott, *Philos. Mag.* **1969**, *19*, 835.
[47] N. Apsley, H. P. Hughes, *Philos. Mag.* **1974**, *30*, 963.
[48] A. Kupferer, S. Vogt, J. Lehnert, F. Munnik, S. Mändl, M. Grundmann, S. G. Mayr, unpublished.
[49] K. Yasuda, J. M. Macak, S. Berger, A. Ghicov, P. Schmuki, *J. Electrochem. Soc.* **2007**, *154*, C472.
[50] Y. V. Bhargava, Q. A. Nguyen, T. M. Devine, *J. Electrochem. Soc.* **2008**, *156*, E62.
[51] S. Berger, S. P. Albu, F. Schmidt-Stein, H. Hildebrand, P. Schmuki, J. S. Hammond, D. F. Paul, S. Reichlmaier, *Surf. Sci.* **2011**, *605*, L57.
[52] S. Plimpton, *J. Comput.Phys.* **1995**, *117*, 1.
[53] M. Matsui, M. Akaogi, *Mol. Simul.* **1991**, *6*, 239.
[54] S. Nosé, *J. Chem. Phys.* **1984**, *81*, 511.
[55] S. Nosé, *Mol. Phys.* **1984**, *52*, 255.
[56] W. G. Hoover, *Phys. Rev. A* **1985**, *31*, 1695.
[57] A. Ricci, G. Ciccotti, *Mol. Phys.* **2003**, *101*, 1927.
[58] J. VandeVondele, M. Krack, F. Mohamed, M. Parrinello, T. Chassaing, J. Hutter, *Comput. Phys. Commun.* **2005**, *167*, 103.
[59] J. VandeVondele, J. Hutter, *J. Chem. Phys.* **2007**, *127*, 114105.
[60] M. Krack, *Theor. Chem. Acc.* **2005**, *114*, 145.
[61] C. Hartwigsen, S. Gœdecker, J. Hutter, *Phys. Rev. B* **1998**, *58*, 3641.
[62] G. Lippert, M. Parrinello, J. Hutter, *Mol. Phys.* **1997**, *92*, 477.
[63] S. Goedecker, M. Teter, J. Hutter, *Phys. Rev. B* **1996**, *54*, 1703.
[64] P. Giannozzi, O. Baseggio, P. Bonfà, D. Brunato, R. Car, I. Carnimeo, C. Cavazzoni, S. D. Gironcoli, P. Delugas, F. F. Ruffino, , A. Ferretti, N. Marzari, I. Timrov, A. Urru, S. Baroni, *J. Chem. Phys.* **2020**, *152*, 154105.
[65] P. E. Blöchl, *Phys. Rev. B* **1994**, *50*, 17953.
[66] V. I. Anisimov, J. Zaanen, O. K. Andersen, *Phys. Rev. B* **1991**, *44*, 943.
[67] M. H. Samat, A. M. M. Ali, M. F. M. Taib, O. H. Hassan, M. Z. A. Yahya, *Res. Phys.* **2016**, *6*, 891.
[68] O. K. Orhan, D. D. O'Regan, *Phys. Rev. B* **2020**, *101*, 245137.
[69] G. Mattioli, P. Alippi, F. Filippone, R. Caminiti, A. A. Bonapasta, *J. Phys. Chem. C* **2010**, *114*, 21694.
[70] J. P. Perdew, K. Burke, M. Ernzerhof, *Phys. Rev. Lett.* **1996**, *77*, 3865.
[71] S. Grimme, S. Ehrlich, L. Goerigk, *J. Comput. Chem.* **2011**, *32*, 1456.
[72] C. G. Broyden, *IMA J. Appl. Math.* **1970**, *6*, 76.
[73] R. Fletcher, *Comput. J.* **1970**, *13*, 317.
[74] D. Goldfarb, *Math. Comput.* **1970**, *24*, 23.
[75] D. F. Shanno, *Math. Comput.* **1970**, *24*, 647.
[76] N. G. Limas, T. A. Manz, *RSC Adv.* **2016**, *6*, 45727.
[77] T. A. Manz, *RSC Adv.* **2017**, *7*, 45552.